J. Fluid Mech. (2007), *vol.* 584, *pp.* 281–299. © 2007 Cambridge University Press
doi:10.1017/S0022112007006611 Printed in the United Kingdom

Effects of polymer stresses on eddy structures in drag-reduced turbulent channel flow

KYOUNGYOUN KIM[1], CHANG-F. LI[2]†, R. SURESHKUMAR[2], S. BALACHANDAR[3] AND RONALD J. ADRIAN[1]

[1]Department of Mechanical and Aerospace Engineering, Arizona State University, Tempe, AZ 85287, USA

[2]Department of Energy, Environmental and Chemical Engineering, Washington University, Saint Louis, MO 63130, USA

[3]Department of Mechanical and Aerospace Engineering, University of Florida, Gainesville, FL 32611, USA

(Received 30 May 2006 and in revised form 11 March 2007)

The effects of polymer stresses on near-wall turbulent structures are examined by using direct numerical simulation of fully developed turbulent channel flows with and without polymer stress. The Reynolds number based on friction velocity and half-channel height is 395, and the stresses created by adding polymer are modelled by a finite extensible nonlinear elastic, dumbbell model. Both low- (18 %) and high-drag reduction (61 %) cases are investigated. Linear stochastic estimation is employed to compute the conditional averages of the near-wall eddies. The conditionally averaged flow fields for Reynolds-stress-maximizing Q2 events show that the near-wall vortical structures are weakened and elongated in the streamwise direction by polymer stresses in a manner similar to that found by Stone *et al.* (2004) for low-Reynolds-number quasi-streamwise vortices ('exact coherent states: ECS'). The conditionally averaged fields for the events with large contribution to the polymer work are also examined. The vortical structures in drag-reduced turbulence are very similar to those for the Q2 events, i.e. counter-rotating streamwise vortices near the wall and hairpin vortices above the buffer layer. The three-dimensional distributions of conditionally averaged polymer force around these vortical structures show that the polymer force components oppose the vortical motion. More fundamentally, the *torques* due to polymer stress are shown to oppose the rotation of the vortices, thereby accounting for their weakening. The observations also extend concepts of the vortex retardation by viscoelastic counter-torques to the heads of hairpins above the buffer layer, and offer an explanation of the mechanism of drag reduction in the outer region of wall turbulence, as well as in the buffer layer.

1. Introduction

Turbulent flows of dilute polymer solutions are known to experience significant reduction of drag relative to the flow of Newtonian fluids under the some conditions. Some of the more important effects that have been established are as follows.

† Present address: School of Energy and Power Engineering, Jiangsu University, Zhenjiang, Jiangsu 212013, P. R. China.

(1) There exist critical values of parameters (e.g. polymer relaxation time and concentration) above which there is onset of drag reduction (DR) (Virk *et al.* 1967; Sreenivasan & White 2000).

(2) A maximum drag reduction (MDR) limit exits, which is known as Virk's asymptote (Virk 1971).

(3) The Reynolds shear stress is reduced significantly, and the total mean stress is larger than the sum of the Reynolds shear stress and the viscous stress. The difference is called the 'stress deficit'. Direct numerical simulations have clearly shown that polymeric stress, arising from the flow-induced stretching of the macromolecules, accounts for the stress deficit. As DR increases, the polymer stress increases significantly, whereas the Reynolds shear stress decreases (Willmarth, Wel & Lee 1987). The stress deficit can also be expressed in terms of an effective viscosity (Sureshkumar, Beris & Handler 1997).

(4) The characteristic length scales, such as the thickness of the buffer region and average streak spacing, increase with increasing DR (Oldaker & Tiederman 1977). Particle image velocimetry (PIV) measurements of White, Somandepalli & Mungal (2004) show the longitudinal scale of the flow to be increased significantly. Analysis by proper orthogonal decomposition (POD) reveals that the dominant modes in drag-reduced flows contain a larger portion of energy, compared to an equivalent Newtonian case (de Angelis *et al.* 2003; Housiadas, Beris & Handler 2005). It is also found that DR hardly changes the shape of the energy-containing modes, but most of the change occurs in the coefficients of the energy-containing modes, not the dissipation modes (de Angelis *et al.* 2003).

(5) In the low-DR ($<35\,\%$) regime, the mean velocity profile is shifted upward with the same slope in the log region. In the high-DR ($>38\,\%$) regime, the slope in the log region is increased. At maximum DR, the buffer region occupies the whole core. Recently, a phenomenological theory of polymer DR has been developed, in which the mean velocity profile at maximum DR is derived theoretically (L'vov *et al.* 2004; Benzi *et al.* 2006). In the low-DR regime, the streamwise turbulent intensity increases with increasing DR, but in the high-DR regime, it decreases with increasing DR (Warholic, Massah & Hanratty 1999). Despite such progress, there is no universally accepted explanation of the mechanism by which very small concentrations of polymer (of order 10–100 p.p.m.) can produce 10–60 % drag reduction.

Over the past decade direct numerical simulations (DNS) of turbulent flows, using various models of non-Newtonian fluid rheology to model the effect of adding polymers, have shown good agreement with experimental observations (Sureshkumar *et al.* 1997; Dimitropoulos *et al.* 1998, 2001; de Angelis, Casciola & Piva 2002; Min *et al.* 2003*a*, *b*; Dubief *et al.* 2004, 2005; Ptasinski *et al.* 2003; Gupta, Sureshkumar & Khomami 2005; Li, Sureshkumar & Khomami 2006*a*). It has been reported that the use of a viscoelastic polymer model is essential to predict the onset of DR and the stress deficit. The most widely used model is based on polymer kinetic theory and utilizes a finitely extensible nonlinear elastic (FENE) dumbbell model of the polymer, i.e. two beads representing hydrodynamic resistance offered by the chain connected by an entropic spring. The stress produced by the model is related to the ensemble average of $\boldsymbol{F}\boldsymbol{Q}$, where $\boldsymbol{F}$ and $\boldsymbol{Q}$ denote the spring force and the end-to-end vector, respectively. In order to obtain a continuum-level constitutive equation for the polymeric stress, closure approximations are employed for the higher moments of $\boldsymbol{Q}$ and the form suggested by Peterlin (1961), leading to the FENE-P model. Despite the simplicity of the model, it qualitatively captures two of the most important features of the flow-microstructure coupling, namely stretching/contraction and orientation by the flow. It has been shown that the two key model parameters, the maximum extensibility L

(i.e. $\boldsymbol{Q} \cdot \boldsymbol{Q} < L^2$) and the relaxation time λ (or equivalently the Weissenberg number (*We*) defined as the ratio of the relaxation time to the characteristic inverse shear rate) can be manipulated to access all of the experimentally observed DR regimes (Li *et al.* 2006*a*).

Recently, several mechanisms of drag reduction by polymer additives have been proposed owing to the successful DNS of the flow. Min *et al.* (2003*b*) derived the transport equation of polymer elastic energy and suggested that the elastic energy stored in the polymers very near the wall is transported to the buffer layer and the log layer and released there. Dubief *et al.* (2004) reported that the polymer work on the flow is highly intermittent in space. Polymers were found to store energy and release it back to the flow. The high intermittency of polymer work is consistent with the polymer effect being associated with the intermittent near-wall structures such as quasi-streamwise and hairpin vortices. Attempts have been made to understand them by using exact coherent states (ECS) models by Graham and co-workers (Stone *et al.* 2002, 2004; Li, Xi & Graham 2006*b*). They have suggested that viscoelasticity has a weakening effect on the streamwise vortices, and for sufficiently low values of the friction Reynolds number (≈ 45), the coherent structures can be suppressed entirely if the elastic effects are sufficiently large. This idea, that the viscoelasticity caused by the polymers weakens vortices that are similar to turbulent vortices, is a powerful, simplifying concept. However, the precise influence of DR on near-wall coherent structures that occurs in fully turbulent flow has not been evaluated.

In the Newtonian flow, the characteristics of wall turbulence such as high- and low-speed streaks, sweep and ejection events, and elevated skin friction are closely related to the near-wall vortical structures in the inner layer (Robinson 1991 and many others) and the outer layer hairpin vortices (Adrian, Meinhart & Tomkins 2000; Ganapathisubramani, Longmire & Marusic 2003). Regarding drag reduction by polymers in the inner layer, de Angelis *et al.* (2002) concluded that 'the viscoelastic reaction exhibits a remarkable level of coherence, associated to the organized motions induced by the coherent structures present in the wall region.' In particular, they discovered that the reaction of the viscoelastic force vector is anti-correlated with turbulent velocity vector except very near the wall. This fundamental observation has been further substantiated for near-wall quasi-streamwise vortices by Stone *et al.* (2004), Dubief *et al.* (2004) and Li *et al.* (2006*a*).

The existing state of knowledge concerning reduction of turbulent drag by dilute polymer solutions focuses almost entirely on the effects of non-Newtonian polymer stresses in the viscous sublayer and buffer layer where turbulent motion is dominated by long, quasi-streamwise vortices and low-speed streaks. As stated above, the principal explanation for the weakening and enlargement of these near-wall vortices is that the body forces due to polymeric stresses oppose the wall-normal and spanwise motions of the vortices (de Angelis *et al.* 2002; Stone *et al.* 2004; Dubief *et al.* 2004; Terrapon *et al.* 2004), either because of the biaxial strain of the molecules in the stagnation-point flow (Terrapon *et al.* 2004) or the strain due to the low-speed streaks (Dubief *et al.* 2004). Recently, Roy *et al.* (2006) also showed by using a low-dimensional model with nine spatial modes (Moehlis, Faisst & Eckhardt 2004) that, at high Weissenberg numbers, polymer forces oppose both biaxial and uniaxial extensional flows and suppress the instability of streaks, thereby the self-sustaining process (Waleffe 1997) becomes weaker.

To continue to improve our understanding of turbulence structure in drag-reducing flow, it is important to examine the details, location and extent of the effects of polymeric stresses on vortical structures in both the near-wall and the outer layer of fully turbulent flow. At low Reynolds number, the viscous layer and the buffer layer

are arguably the most important regions for drag reduction because the majority of the mean velocity change occurs across them. But, at higher Reynolds number, where many real applications reside, a significant fraction of the velocity rise occurs above the buffer layer, making it necessary to understand the effects of polymers in that region, as well. To this end, the present study examines the vortices in $Re_\tau = 395$ channel flow with drag reduction of 0 %, 18 % and 61 % based on a FENE-P model, as in Li *et al.* (2006*a*). The higher Reynolds number ensures that there is room for hairpin eddies and other three-dimensional eddies to form in the outer layer.

To achieve a clearer picture of the relationship between the eddies and the polymer stresses, we use stochastic estimation based on the two-point correlation tensor of velocity, to find conditional eddies associated with the large Q2 events that typify the production of Reynolds shear stress in the buffer layer and in the outer layer. To connect with previous work, the relationships between the polymer body force and the conditional eddies are presented, and we find strong evidence to support the idea that polymer stress counteracts the near-wall vortices. The simplicity of the conditional eddies, relative to the complexity of instantaneous fields (cf. figure 8 in Dubief *et al.* 2005, for example), also makes it possible to determine the details of the polymer force distribution around an eddy. To put these ideas on a more fundamental mechanical basis, we explore how the *torques* due to polymer stress are distributed around the quasi-streamwise vortices and the heads and legs of hairpins. The torques are the source of weakening of the eddies in the equation for mean square vorticity and, as such, they are more important than forces in determining the overall mechanism and affecting turbulent transport. Finally, we show that the counter-torques created by straining the polymers also inherently oppose the rotation of the legs and heads of the hairpins, i.e. the elements responsible for generating much of the Reynolds shear stress in the logarithmic layer. Thus, even if the near-wall layer were to be destroyed by, say, roughness of the wall, there is still a mechanism by which polymers can reduce turbulent momentum transport.

2. Governing equations and numerical method

The non-dimensional governing equations of unsteady, incompressible, viscoelastic flow with the FENE-P model are given by

$$\frac{\partial u_i}{\partial x_i} = 0, \tag{2.1}$$

$$\frac{\partial u_i}{\partial t} + u_j \frac{\partial u_i}{\partial x_j} = -\frac{\partial p}{\partial x_i} + \frac{\beta}{Re_{\tau o}} \frac{\partial^2 u_i}{\partial x_j^2} + \underbrace{\frac{(1-\beta)}{Re_{\tau o}} \frac{\partial \tau_{ij}}{\partial x_j}}_{f_i} + \delta_{i1}, \tag{2.2}$$

$$\frac{\partial c_{ij}}{\partial t} + u_k \frac{\partial c_{ij}}{\partial x_k} = c_{ik} \frac{\partial u_j}{\partial x_k} + \frac{\partial u_i}{\partial x_k} c_{kj} - \underbrace{\frac{Re_{\tau o}}{We_{\tau o}} \left(\frac{L^2 - 3}{L^2 - c_{kk}} c_{ij} - \delta_{ij} \right)}_{\tau_{ij}}, \tag{2.3}$$

where u_i is the velocity, p is the pressure, and τ_{ij} is the polymer stress. The friction velocity u_τ and the channel half-height h are used as the velocity and length scale, respectively. The Reynolds number is defined as $Re_{\tau o} = u_\tau h / \nu_o$, where ν_o is the zero-shear-rate kinematic viscosity of the solution. The parameter β is the ratio of the solvent viscosity (μ_s) to the total solution zero-shear-rate viscosity (μ_o). The polymer stress tensor, τ_{ij}, is made dimensionless using $\mu_{po} u_\tau / h$, where $\mu_{po} = \mu_o - \mu_s$ is the polymer contribution to the total zero-shear-rate viscosity of solution. The last term in (2.2) is referred to as the polymer body force, f_i, and it arises from the polymer

	Newtonian	Low DR	High DR
DR(%)	–	18	61
$We_{\tau o}(=\lambda u_\tau^2/\nu_o)$	–	25	100
L^2	–	900	14400
β	–	0.9	0.9
$L_x \times L_z$	$2\pi h \times \pi h$	$4\pi h \times 0.5\pi h$	$8\pi h \times 0.5\pi h$
$L_x^+ \times L_z^+$	2482×1241	4964×620	9927×620
Grid	$128 \times 129 \times 128$	$128 \times 129 \times 64$	$256 \times 129 \times 64$
$\Delta t u_\tau / h$	2×10^{-4}	2×10^{-4}	1×10^{-4}

TABLE 1. Simulation details.

stress. The polymer stress, τ_{ij}, is obtained by solving an evolution equation for the conformation tensor, c_{ij}, which is the average second moment of the polymer chain end-to-end distance vector. It has maximum dimensionless extensibility L^2. Note that c_{ij} and L^2 are made dimensionless by kT/H, where k, T and H denote the Boltzmann constant, the absolute temperature and the Hookean dumbbell spring constant, respectively. In the FENE-P model, the polymer stress is related to the departure of the conformation tensor from its equilibrium state as expressed in (2.3). The Weissenberg number $We_{\tau o} = \lambda u_\tau^2/\nu_o$ is the ratio of the polymer relaxation time, λ, to the flow time scale.

The numerical method used for solving the governing equations is described in detail in Li *et al.* (2006*a*). Time integration of the governing equations is achieved by a semi-implicit method. In space, a fully spectral method is used with Fourier representations in the streamwise and spanwise directions, and Chebyshev expansion in the wall-normal direction. In order to achieve stable numerical integration of the evolution equation for the conformation tensor, a stress diffusion term $D\partial^2 c_{ij}/\partial x_k^2$ is introduced in (2.3), where $D = \kappa/hu_\tau$, and κ denotes a constant, isotropic, artificial numerical diffusivity. As in earlier studies (Sureshkumar *et al.* 1997; Dimitropoulos *et al.* 1998), the dimensionless artificial numerical diffusivity D is taken to be of $O(10^{-2})$. The boundary condition for c_{ij} at the wall is imposed as the result of integrating (2.3) without the diffusion term (Dimitropoulos *et al.* 1998). Periodic boundary conditions are applied in the streamwise and spanwise directions, and the no-slip boundary condition is imposed on velocity at the solid walls. For the Newtonian flow ($Re_{\tau o} = 395$), the simulation domain is $2\pi h \times 2h \times \pi h$ ($2500 \times 790 \times 1250$ in wall units) in the streamwise, wall-normal and spanwise directions, respectively. For this DR flow, a larger streamwise domain is required, since drag reduction is accompanied by an increase in streamwise correlation length. Note that simulation of MDR flow with a small streamwise domain results in laminar flow (Li *et al.* 2006*a*), contradicting experimental observation of sustained turbulence even in the MDR regime (Warholic *et al.* 1999). In the present DR simulations, the streamwise computational domain was chosen to be either two or four times longer than that for the Newtonian flow, as needed. Details of the polymer parameters and grid resolutions in the simulations are listed in table 1.

3. Stochastic estimation

The effects of polymer additives on the characteristic near-wall flow structures are investigated by examining the conditionally averaged flow field around them. With an appropriate choice of the event (or condition) in the conditional average,

attention can be focused on different types of near-wall coherent structures. A true conditional average is statistically very hard to obtain, especially when the condition is multidimensional. Here, we approximate the conditional averages by linear stochastic estimation (Adrian 1996). The conditional average of a fluctuating quantity, $g_i(\boldsymbol{x}, t)$, given a set of one-point events or conditions, $E_j(\boldsymbol{x}', t)$ ($j = 1, \ldots, N$, where N is the total number of conditions specified at the point $\boldsymbol{x}'$) is denoted as $\langle g_i|\boldsymbol{E}\rangle$. Given $E_j(\boldsymbol{x}', t)$, the conditional average is the best estimate for $g_i(\boldsymbol{x}, t)$, in the sense of minimum mean square error. Linear stochastic estimation approximates conditional averages in a form that is computationally convenient, since it depends only on unconditional averages. The accuracy of linear stochastic estimation as an approximation to conditional average has been reported elsewhere (Adrian *et al.* 1989).

The linear stochastic approximation of the conditional average $\langle g_i|\boldsymbol{E}\rangle$ is written as

$$\hat{g}_i(\boldsymbol{x}, t) = L_{ij}(\boldsymbol{x}, \boldsymbol{x}')E_j(\boldsymbol{x}', t). \tag{3.1}$$

Choosing L_{ij} to minimize the mean square error yields equations for L_{ij} in terms of unconditional, two-point, second-order spatial correlation tensors:

$$\langle E_j(\boldsymbol{x}')E_k(\boldsymbol{x}')\rangle L_{ij} = \langle g_i(\boldsymbol{x})E_k(\boldsymbol{x}')\rangle, \tag{3.2}$$

where the angle brackets represent the ensemble average.

4. Results

4.1. *Turbulent vortical structures in DR flows*

Figure 1 shows the wall vortical structures detected by plotting isosurfaces of swirling strength, λ_{ci}. Swirling strength is defined as the imaginary part of the complex conjugate eigenvalues of the local velocity gradient tensor (Zhou *et al.* 1999; Chakraborty, Balachandar & Adrian 2005). The swirling strength extracts compact vortical cores and discriminates against regions of shear. In figure 1(*a*), the number of vortices with intense swirling strength decreases with increasing DR. For the DR = 61 % case, vortices with $\lambda_{ci}\nu/u_\tau^2 = 0.1$ totally disappear and vortices with lower swirling strength are detected more intermittently. In the viscoelastic flows the vortical structures are significantly weaker than in the Newtonian flow. This weakening is one of the key features of reduced-drag wall-bounded turbulent flows (Choi, Moin & Kim 1993, 1994; Lim, Choi & Kim 1998). Figure 1(*b*) shows isosurfaces of the swirling strength relative to its maximum in each domain. As DR increases, vortices thicken and their streamwise lengths increase, while their strengths weaken (figure 1*a*). The streamwise length scale of turbulent structures is also observed to increase in experiments (White *et al.* 2004).

It is known that coherent near-wall structures are closely related to the production of Reynolds shear stress (Robinson 1991). In drag-reducing flow, experimental results show that the Reynolds shear stress decreases significantly (Wei & Willmarth 1992; Warholic *et al.* 1999; Ptasinski *et al.* 2001). We have examined the changes of the vortical structures that occur as Reynolds shear stress decreases in the viscoelastic flows. To obtain the conditional averaged flow fields associated with the Reynolds stress, we follow the method of Moin, Adrian & Kim (1987) (cf. also Kendall 1992; Zhou *et al.* 1999). A second-quadrant (Q2) event at a given y location is chosen as the event for the linear stochastic estimation. These Q2 events $(E_1, E_2) = (u_m, v_m)$ are found by detecting the values of $u' = u_m$ and $v' = v_m$ that maximize the probability-weighted Reynolds shear stress $u'v'$ p.d.f.(u', v'), i.e., which have largest contribution to the mean Reynolds shear stress.

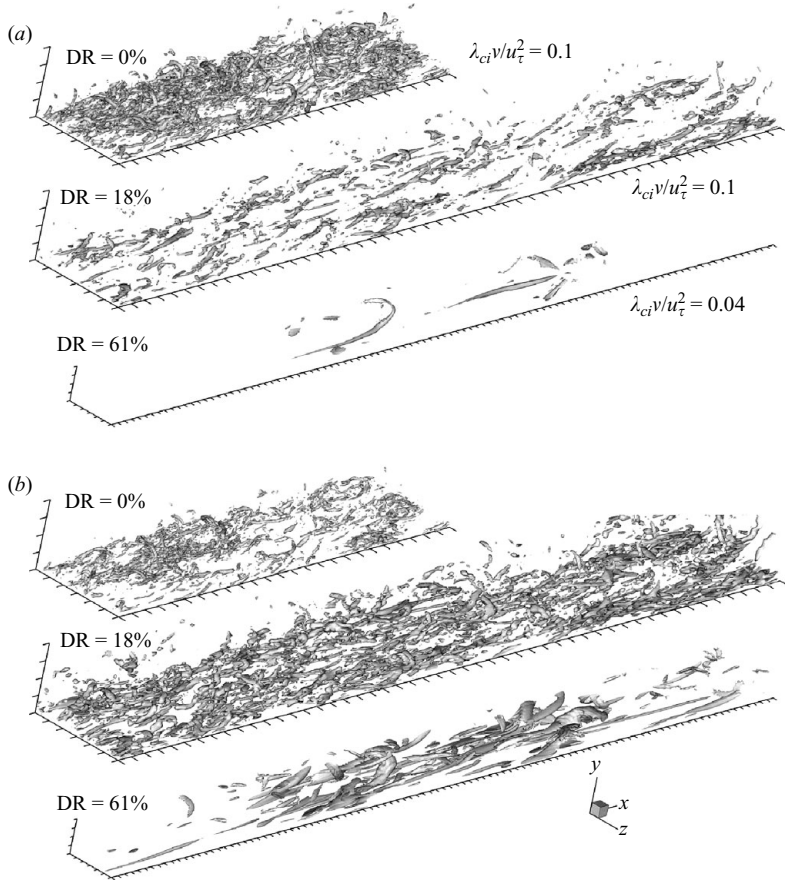

FIGURE 1. Near-wall vortical structure in the drag-reducing flow with polymer additives. The distance between ticks on each axis is 100 wall units. The same instantaneous flow fields are used in both (*a*) and (*b*) for each DR case. (*a*) Contours of non-dimensionalized swirling strength $\lambda_{ci}\nu/u_\tau^2$; (*b*) contours of 20 % of maximum λ_{ci}.

Figures 2(*a*)–2(*f*) show the isosurfaces of λ_{ci} for the stochastically estimated velocity field of the Q2 event specified at y locations between $5.8 \leqslant y^+ \leqslant 200$. The conditional eddies given Q2 events very near the wall ($y^+ \leqslant 19.9$) are counter-rotating pairs of streamwise vortices that induce ejections between them. Further away from the wall ($y^+ \geqslant 30.1$), the conditional eddies given Q2 events are hairpin vortices. As DR increases, the streamwise lengths of the counter-rotating streamwise vortices increase and the spanwise spacing between the centre of each streamwise vortex pair also increases. For the hairpin vortices, the legs of the hairpins in the non-Newtonian flows are more elongated and bigger than those of the Newtonian flow. The inclination angles of the vortex legs become smaller with increased DR. We have also stochastically estimated the velocity field for the DR cases using the same event vector as for the Newtonian case and the results (not shown here) show that the inclination angle of the vortex legs is still smaller in the DR case. This behaviour is consistent with the observation that the addition of polymers causes the flow to be more parallel to the wall (Warholic *et al.* 2001).

Since two-dimensional events $(u_m, v_m, 0)$ are used in the estimation, the estimated flow structures (figures 2*a*–2*f*) are symmetric about the $z = 0$. Asymmetric structures

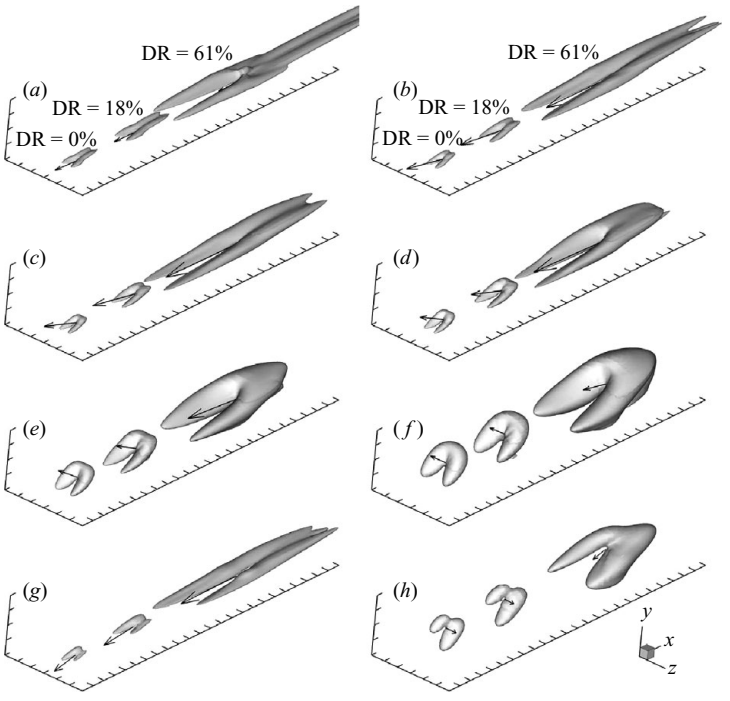

FIGURE 2. Vortical structures of the linearly estimated flow field with the Q2 event $\boldsymbol{u}' = (u_m, v_m, 0)$: (*a*) $y^+ = 5.8$; (*b*) $y^+ = 19.9$; (*c*) $y^+ = 30.1$; (*d*) $y^+ = 51.3$; (*e*) $y^+ = 102$; (*f*) $y^+ = 200$. Asymmetric structures in the linearly estimated flow field with the event $\boldsymbol{u}' = (u_m, v_m, 2v_m)$: (*g*) $y^+ = 19.9$; (*h*) $y^+ = 200$. The structures corresponding to the DR = 0 %, 18 % and 61 % case are displayed in ascending order of DR in the streamwise direction. The vortices are identified with an isosurface of swirling strength (35 % of maximum λ_{ci}). The vectors represent the velocity events used in the estimation. The distance between ticks on each axis is 100 wall units.

can also be detected by using an event with non-zero w component in addition to Q2 events. Figures 2(*g*) and 2(*h*) show the asymmetric flow structure associated with the event $(u_m, v_m, 2v_m)$ at $y^+ = 19.9$ and 200, respectively. As in the case of symmetric structures, these asymmetric structures are bigger and more elongated in the streamwise direction as DR increases.

4.2. *Vortical structures educed by polymer work events*

To see the effects of polymer additives on the turbulence, we consider the budget equations for the kinetic energy of each turbulent velocity fluctuations ($i = 1, 2, 3$, no summation on i):

$$\frac{\bar{D}\left\langle \frac{1}{2}u_i'^2 \right\rangle}{\bar{D}t} = -\langle u_i' u_2' \rangle \frac{\mathrm{d}\langle u_i \rangle}{\mathrm{d}y} - \frac{\beta}{Re}\left\langle \frac{\partial u_i'}{\partial x_k}\frac{\partial u_i'}{\partial x_k} \right\rangle + \langle u_i' f_i' \rangle + \frac{\mathrm{d}}{\mathrm{d}y}\left(-\left\langle \frac{1}{2}u_i'^2 u_2' \right\rangle + \frac{\beta}{Re}\frac{\mathrm{d}}{\mathrm{d}y}\left\langle \frac{1}{2}u_i'^2 \right\rangle \right) + \left\langle u_i' \frac{\partial p'}{\partial x_i} \right\rangle, \tag{4.1}$$

where $(\bar{D}(\cdot))/(\bar{D}t) = \langle u_k \rangle (\partial(\cdot))/(\partial x_k)$. In (4.1), the 'polymer work' appears as the correlation between velocity fluctuations and polymer force fluctuations, $E_i = \langle u_i' f_i' \rangle$. Negative (positive) E_i means the energy carried by velocity fluctuations u_i' is dampened (enhanced) by storage (release) of elastic energy in the polymers. Figure 3 shows the

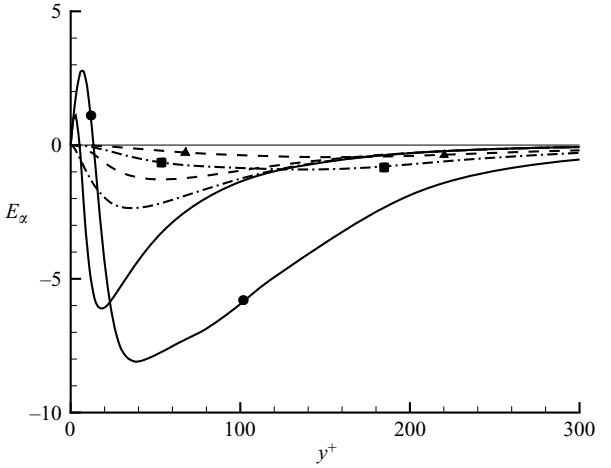

FIGURE 3. Profiles of polymer work: $E_x = \langle u' f_x' \rangle$ (——); $E_y = \langle v' f_y' \rangle$ (— — —); $E_z = \langle w' f_z' \rangle$ (— · — · —). Lines only: DR = 18 %; Lines with symbols: DR = 61 %.

profiles of the values of polymer work term E_i. In the $\langle u'^2 \rangle$ equation, E_x has positive values in the viscous sublayer and negative values away from the wall. This is consistent with the findings of de Angelis *et al.* (2002) and Li *et al.* (2006*a*) that the correlation of u' and f_x' is positive very close to the wall but changes its sign away from the wall. However, E_y and E_z are always negative, consistent with the findings that polymer forces oppose the fluid motion around the near-wall streamwise vortices (Stone *et al.* 2004; Dubief *et al.* 2005). As DR increases, the maximum and minimum values of E_x increase in magnitude while the magnitudes of E_y and E_z decrease. The locations of all extrema of E_i shift away from the wall with increased DR.

To understand the polymer work further, we have examined the joint probability density function of u_i' and f_i' at the y locations of the local minimum and the maximum of E_i. Very close to the wall, large positive values of the streamwise polymer work are detected more *frequently* in the high-speed streaks, consistent with Dubief *et al.* (2004). However, we found that the event *making the largest positive contribution* to E_x occurs in the low-speed streak. The location of the maximum in the contour plot of $u_i' f_i'$p.d.f.(u_i', f_i') corresponds to the values of u_i' and f_i' that contribute most to the mean polymer work E_i.

To see the flow structures associated with polymer work, we examined the conditional averages of the flow fields associated with the events contributing most to the polymer work:

$$\langle \boldsymbol{u}(\boldsymbol{x}) | u_i' = a_m \text{ and } f_i' = b_m \text{ at the } y \text{ location of maximum or minimum } E_i \rangle. \quad (4.2)$$

The conditional fields are obtained by linear stochastic estimation with the events summarized in table 2. Figures 4(*a*) and 4(*b*) show the vortical structures corresponding to the event contributing most to E_x at the locations of maximum and minimum E_x. The estimated structures are nearly the same as those associated with large Q2 event at similar y locations in figures 2(*a*)–2(*b*). Closer inspection of figures 4(*a*) and 4(*b*) reveals that between streamwise vortices, positive E_x is located very close to the wall while the locations of negative E_x are farther away from the wall, at nearly the same as y location as the maximum of $\omega_{x,\mathrm{rms}}$ (not shown here). Figure 4(*c*) shows the vortical structures associated with negative polymer work E_y

DR		y^+	a	b	$a_{\rm rms}$	$b_{\rm rms}$	$a_m/a_{\rm rms}$	$b_m/b_{\rm rms}$
18 %	maximum E_x	2.97	u'	f_x'	1.08	4.87	−1.20	−0.60
	minimum E_x	17.01	u'	f_x'	2.92	5.66	−1.60	0.60
	minimum E_y	51.32	v'	f_y'	0.79	3.28	1.20	−0.60
	minimum E_z	33.89	w'	f_z'	1.12	4.08	1.20	−0.60
61 %	maximum E_x	7.59	u'	f_x'	2.13	6.22	−1.60	−0.60
	minimum E_x	37.92	u'	f_x'	4.45	6.32	−1.80	0.40
	minimum E_y	159.70	v'	f_y'	0.45	3.01	0.80	−0.20
	minimum E_z	137.00	w'	f_z'	0.65	3.64	1.00	−0.20

TABLE 2. Values of u_i' and f_i' at the locations of maximum contribution to the polymer work. For the cross-stream components, the events are chosen with positive velocity fluctuations.

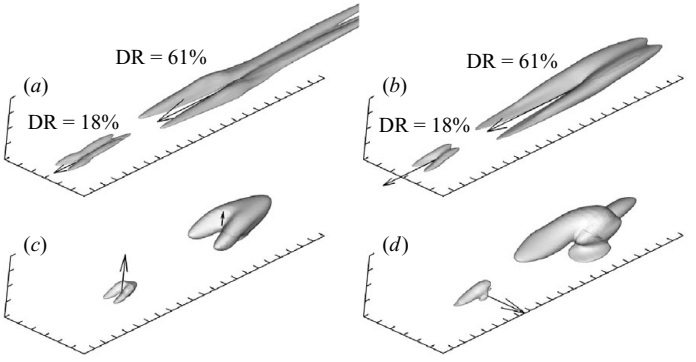

FIGURE 4. Conditional eddies given the event (u_i', f_i') at the y location of (a) the positive maximum of E_x, (b) the negative maximum of E_x, (c) the negative maximum of E_y, (d) the negative maximum of E_z. The structures corresponding to the DR = 18 % and 61 % case are displayed in ascending order of DR in the streamwise direction. The eddies are identified with an isosurface of swirling strength (35 % of maximum λ_{ci}). The vectors indicate only velocity u_i' of the event (u_i', f_i') in table 2. The distance between ticks on each axis is 100 wall units.

at its minimum locations. Figures 4(a)–4(c) show that the vortical structures related to the polymer works E_x and E_y are very similar to those for the Q2 events (figure 2). Figure 4(d) shows the flow structures corresponding to the event contributing most to E_z. The signs of the upper and lower streamwise vortices oppose each other, and the vortices induce large positive spanwise velocity and negative spanwise polymer force in the overlapped region. Because these structures are from the conditionally averaged flow field regardless of the sign of u' and v', these asymmetric structures show different shapes from those in figures 2(g) and 2(h). The eddies are weaker and bigger as DR increases, similar to the behaviour of the eddies detected by the Q2 event in figure 2.

4.3. *Distribution of polymer forces and torques around turbulent vortical structures*

Dubief *et al.* (2005) showed isosurfaces of each component of polymer force (f_i') and vortical structures for one three-dimensional realization, and the visualization clearly indicated that polymer forces cluster in the immediate neighbourhood of near-wall vortices. However, it is hard to interpret the anti-correlation between polymer force and velocity from visualization of a random field because the instantaneous flow field is too complicated. Stone *et al.* (2004) showed the distribution of polymer forces

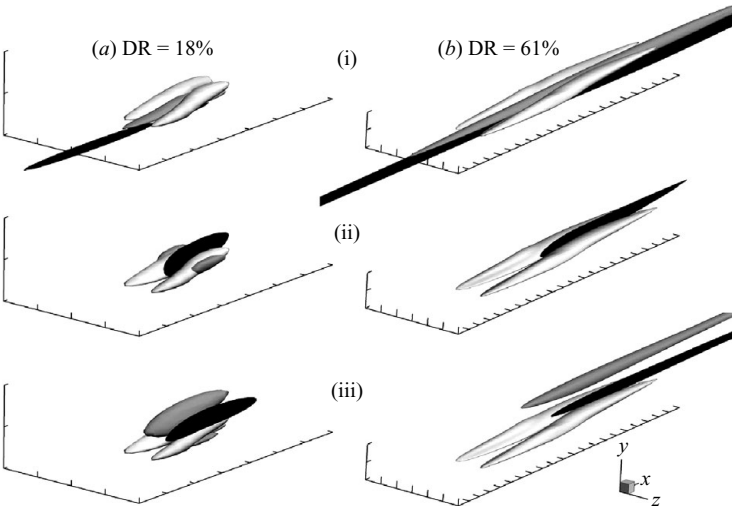

FIGURE 5. Isosurfaces of conditional polymer force components (*i*) f_x', (*ii*) f_y' and (*iii*) f_z' around the eddy structure at $y^+ = 19.9$. (*a*) DR = 18 %. (*b*) DR = 61 %. The grey and black surfaces denote positive and negative values of polymer force, respectively. The isosurface levels of polymer force are (*a*): (*i*) $f_x' = \pm 1.0$ (*ii*) $f_y' = \pm 0.4$ (*iii*) $f_z' = \pm 0.4$; (*b*): (*i*) $f_x' = \pm 1.0$ (*ii*) $f_y' = \pm 0.3$ (*iii*) $f_z' = \pm 0.45$. White surfaces show the vortices identified with 35 % of maximum λ_{ci}. The distance between ticks on each axis is 100 wall units.

(f_y', f_z') and velocity fluctuations (v', w') for the ECS. Since the ECS is smoother and simpler than a three-dimensional realization at high *Re*, it was possible to clearly see that (f_y', f_z') opposes (v', w') motion of the quasi-streamwise vortices in the ECS. However, the Reynolds number of the ECS was low. In the present study, owing to the conditional averages, we are able here to explore the relationship between the full three-dimensional polymer force fields and conditional eddies of fully turbulent flow. Our findings support and give detail to those of Dubief *et al.* (2005) and Stone *et al.* (2004). Furthermore, we find a simpler and more basic mechanistic interpretation in terms of non-Newtonian *torques* that inherently oppose the rotation of the vortices, both quasi-streamwise vortices and hairpin (ω_z').

To investigate the distribution of polymer forces around the counter-rotating pair of streamwise vortices, the isosurfaces of the stochastically estimated polymer forces are displayed in figure 5. Figures 5*a*(*i*) and 5*b*(*i*) show the isosurface of the streamwise component of polymer force around the vortical structure of the estimated flow fields given a Q2 event at $y^+ = 19.9$. The counter-rotating pair of streamwise vortices induce negative streamwise velocity fluctuations which result in a low-speed streak between each vortex. Positive f_x' is detected between the streamwise vortices, where negative u' is induced, while a region of negative f_x' is observed very close to the wall. This is consistent with the polymer work E_x profiles which has negative value except very near the wall in figure 3. Figures 5*a*(*ii*) and 5*a*(*iii*) show the isosurface of wall-normal and spanwise components of polymer force around the vortex pair for the DR = 18 % case. The streamwise elongated regions of strong vertical polymer force (f_y') are observed along either side of the streamwise vortices, while elongated regions of strong spanwise polymer force (f_z') occur above and below the streamwise vortices. The vortex pair associated with the ejection induces positive wall-normal velocity fluctuations between each vortex and negative v' along outer flanks of vortices. Considering the location

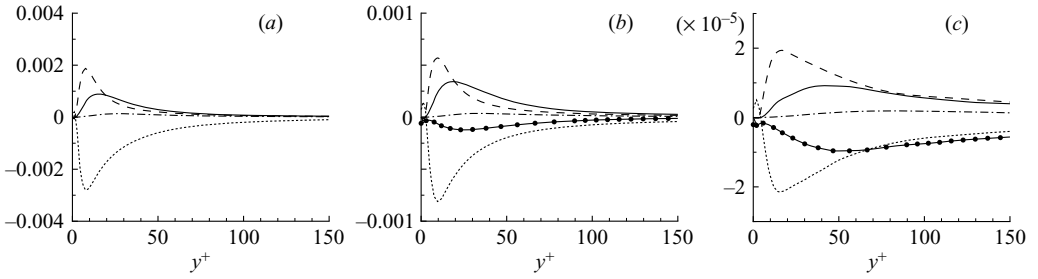

FIGURE 6. Time- and x–z-plane-averaged terms normalized by u_τ^6/ν^3 in the transport equation of ω_x^2: *ST* (——); TT_1 (– – –); TT_2 (– · – · –); *DF* (· · · · · ·); *VE* (—•—). (*a*) DR = 0 %; (*b*) DR = 18 %; (*c*) DR = 61 %. See (4.3) for the definition of the different terms.

of upwelling and downwelling flow associated with the vortices, the distributions of f_y' and f_z' show the polymer force directly counteracting the fluid motion around the streamwise vortices. For DR = 61 %, shown in figures 5*b*(*ii*) and 5*b*(*iii*), the behaviour is similar. These results, based on DNS, are consistent with the findings that the velocity and polymer force are anti-correlated around the counter-rotating pairs of streamwise vortices in exact coherent state models (*cf.* figure 14 of Stone *et al.* 2004).

The opposition of polymer forces to Reynolds-stress-producing motions is a fundamental mechanism for reducing Reynolds shear stress and drag. Taking one step further, given that much of the Reynolds stress is created by vortices, one can ask how polymer stresses inhibit vortex motion. To investigate the effect of polymer additives on the strength of streamwise vortices, the following equation for the square of streamwise vorticity is examined:

$$\frac{1}{2}\frac{\mathrm{D}\omega_x^2}{\mathrm{D}t} = \underbrace{\omega_x^2\frac{\partial u}{\partial x}}_{ST} - \underbrace{\omega_x\frac{\partial w}{\partial x}\frac{\partial u}{\partial y}}_{TT_1} + \underbrace{\omega_x\frac{\partial v}{\partial x}\frac{\partial u}{\partial z}}_{TT_2} + \underbrace{\omega_x\frac{\beta}{Re_{\tau o}}\nabla^2\omega_x}_{DF} + \underbrace{\omega_x\left(\frac{\partial f_z}{\partial y} - \frac{\partial f_y}{\partial z}\right)}_{VE}. \tag{4.3}$$

The first four terms on the right-hand side of (4.3) represent: ST = contribution due to stretching of ω_x, TT_1 = net contribution due to the tilting of ω_y, TT_2 = net contribution due to the twisting of ω_z, DF = diffusion. The polymer effect appears in the last term (VE), which represents the work done by the torque of the polymer force field. Figure 6(*a*) shows the time- and x–z-plane-averaged values of the different terms of (4.3) in the Newtonian flow. TT_2 is negligible compared with the other three terms (ST, TT_1 and DF), consistent with the results of Brooke & Hanratty (1993). For $y^+ < 10$, the tilting term (TT_1) dominates, whereas the stretching term has nearly the same magnitude as the tilting term for $y^+ > 20$. For the high-DR (= 61 %) case, TT_1 dominates over a much larger distance from the wall, and it remains comparable to ST throughout the channel, while for low-DR (= 18 %), the profiles of TT_1 and ST are similar to those for the Newtonian case. In both drag-reducing flows (figures 6*b* and 6*c*), the polymer contribution (VE) is negative. Since VE represents the correlation of $(\nabla \times \boldsymbol{u})_x$ and $(\nabla \times \boldsymbol{f})_x$, a negative value implies that *the polymer torque acts in the opposite direction to the vorticity*, and thus it reduces the strength of the vortex. At DR = 61 %, the negative contribution of VE to streamwise vorticity is relatively much larger than in the lower DR case, thus explaining the significantly reduced strength of vortical structures that occur at higher drag reduction. The profiles of other terms

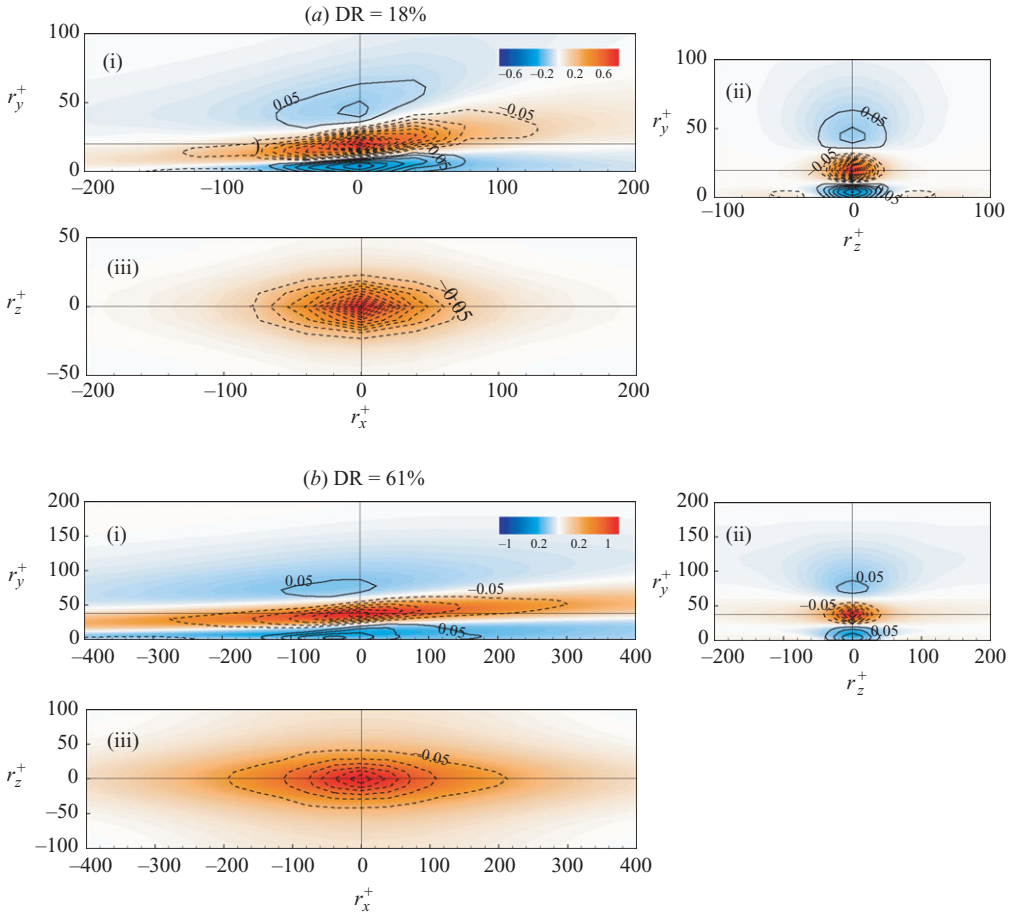

FIGURE 7. Two-point cross-correlation coefficient between streamwise vorticity fluctuations at (x, y_0, z) and streamwise polymer torque fluctuations at $(x + r_x, r_y, z + r_z)$ for (*a*) DR = 18 %, $y_0^+ = 19.9$, and (*b*) DR = 61 %, $y_0^+ = 37.9$. Contours are plotted in the (i) x–y plane at $r_z^+ = 0$, (ii) y–z plane at $r_x^+ = 0$, (iii) x–z plane at $r_y^+ = y_0^+$. The increment of contour levels is 0.05. Negative contours are dashed and zero contours are not drawn. Flooded contours represent $R_{\omega_x'\omega_x'}$.

show similar behaviour; however, the magnitudes are reduced owing to the weakened vortex.

To examine the spatial distribution of polymer torque around the near-wall streamwise vortex, two-point cross-correlation coefficients between ω_x' and streamwise polymer torque fluctuations $\mathscr{T}_x' = (\nabla \times \boldsymbol{f}')_x$ have been calculated:

$$R_{\omega_x'\mathscr{T}_x'}(r_x, r_y, r_z; y_0) = \frac{\langle \omega_x'(x, y_0, z)\mathscr{T}_x'(x + r_x, r_y, z + r_z)\rangle}{\omega_{x,\mathrm{rms}}'(y_0)\,\mathscr{T}_{x,\mathrm{rms}}'(r_y)}, \tag{4.4}$$

where the reference location, y_0, is chosen as the location of local maximum in the $\omega_{x,\mathrm{rms}}'$ profile. Figure 7 shows contours of $R_{\omega_x'\mathscr{T}_x'}$ plotted on the three mutually perpendicular planes for DR = 18 % and 61 %. To indicate the location of the streamwise vortex, the auto-correlation of streamwise vorticity fluctuations, $R_{\omega_x'\omega_x'}$ is also shown by flooded contours. Strong negative values of $R_{\omega_x'\mathscr{T}_x'}$ occur around the

vortex core. They are elongated in the streamwise direction with an inclination angle similar to the auto-correlation of ω_x'. The negative correlations show that *the polymer torque acts counter to streamwise vortical motions throughout the region of the core*. This is consistent with the mean negative contribution of the polymer torque to $\omega_x'^2$ in figure 6. Positive correlations of $R_{\omega_x'\mathscr{T}_x'}$ appear above and below the streamwise vortex centre, coincident with negative values of the auto-correlation of ω_x'. Since negative $R_{\omega_x'\omega_x'}$ indicates rotations counter to those of the central vortex, the positive correlations of $R_{\omega_x'\mathscr{T}_x'}$ indicates that *the torque acts counter to the vortical motion in these regions*, also. As DR increases, the correlation contour becomes more elongated in the streamwise direction and wider in the spanwise direction. The magnitude of $R_{\omega_x'\mathscr{T}_x'}$ decreases owing to reduced $\omega_{x,\mathrm{rms}}'$ as DR increases.

Above the buffer layer, the hairpin vortices become more common than quasi-streamwise vortices (*cf.* figure 2). To see the distribution of polymer forces around the hairpin vortex, the polymer body forces around the vortical structure of the stochastically estimated flow fields given a Q2 event at $y^+ = 102$ are examined. The distribution of polymer body force, the velocity and polymer force vectors on the x–y and y–z planes are displayed in figure 8. In the x–y plane located at $z^+ = 0$, it is clear that, immediately upstream of the hairpin vortex head, the polymer force inhibits the Q2 pumping of the hairpin vortex. For both DR cases, the streamwise component of polymer force is directed in the negative streamwise direction very close to the wall. This is consistent with positive correlation between f_x' and u' in the vicinity of the wall (de Angelis *et al.* 2002). In the y–z plane located at $x^+ = 0$, the velocity vectors show a counter-rotating vortical motion around the vortex legs, and the polymer force vectors also show a counter-rotating pattern that is opposite in direction to the vortex pair. The centres of the polymer force patterns deviate from the centres of the velocity vector plots. For example, in the case of DR = 18 %, the centre of the polymer force is located at $y^+ = 80$, below that of fluid motion located at $y^+ = 110$. The spanwise separation between the centres of polymer force patterns is $\Delta z^+ = 70$, as compared with $\Delta z^+ = 145$ for the velocity patterns. Flooded contours of the swirling strength provide another means of locating the cores of the hairpin vortex. The polymer force pattern is in better alignment with the swirling strength pattern than the velocity vector pattern, but the relationship between the vortex pattern and the polymer force pattern is still not simple enough to conclude that the polymer force uniformly retards the vortex motion everywhere. Better evidence for vortex retardation is found by comparing the pattern of vorticity–vorticity correlation with the vorticity–torque correlation: figure 9. As with the comparison in figure 7, the plot shows that the polymer torque is clearly *anti-correlated* with the spanwise vorticity around the core of the hairpin head.

The present results show that the modified vortical structures due to the polymer additives and distribution of polymer forces around the vortices are qualitatively similar between low- and high-drag reduction cases, although the mean velocity profiles appear fundamentally different in the low- and high-drag regimes, as stated in the Introduction.

5. Summary and conclusions

The effects of polymer additives on the structure of eddies in wall turbulence have been investigated by analysing direct numerical simulations (Li *et al.* 2006*a*) of fully developed turbulent channel flows with and without polymer additives. The analysis uses two-point spatial correlations and linear stochastic estimation to find the

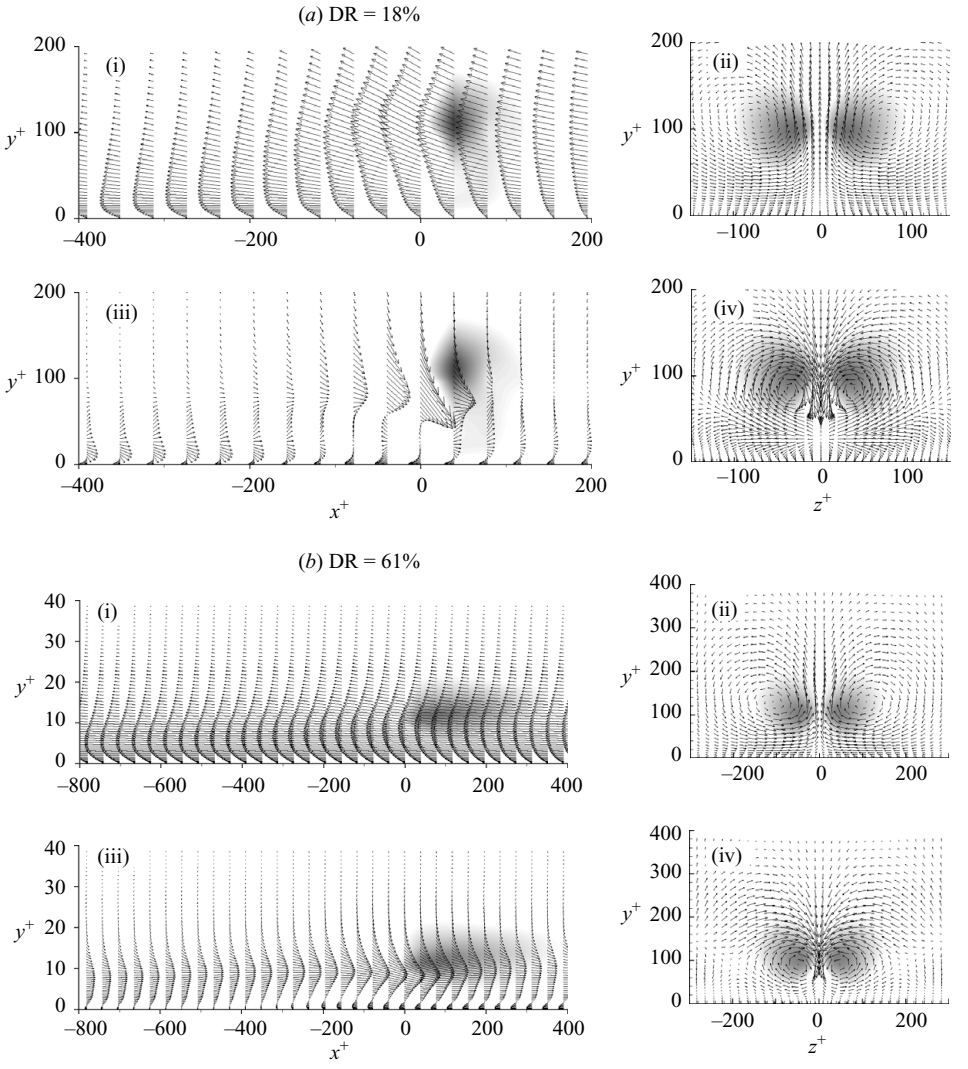

FIGURE 8. Velocity and polymer body force vectors on the x–y and y–z planes at $z^+ = 0$ and $x^+ = 0$, respectively. (i) (u',v') (ii) (w',v') (iii) (f_x',f_y') (iv) (f_z',f_y'). Flooded contours of λ_{ci} are also overlaid, with dark regions indicating large swirling strength.

patterns of velocity, vorticity, polymer force and polymer torque in the conditional eddies. The polymer stress is modelled using a FENE-P dumbbell model and the Reynolds number based on friction velocity and half-channel height is 395. Both low-DR (18 %) and high-DR (61 %) cases were investigated and compared to the results for Newtonian flow.

The changes of the vortical structures associated with decreased Reynolds shear stress are examined by linear stochastic estimation for the second-quadrant (Q2) event that makes the maximum contribution to mean second-quadrant Reynolds shear stress. Given a Q2 event at $y^+ \leqslant 19.9$, the conditional eddies are found to be a pair of counter-rotating streamwise vortices. Given Q2 events at $y^+ \geqslant 30$, the conditional eddies resemble hairpins. As DR increases, the conditional eddies become more elongated and bigger and the inclination angles of the vortex legs become

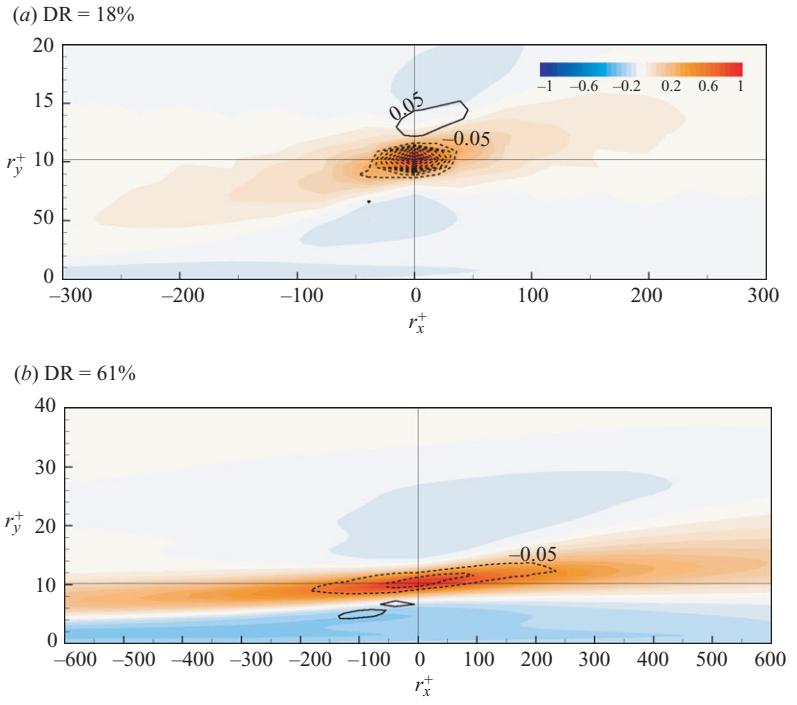

FIGURE 9. Two-point cross-correlation coefficient between spanwise vorticity fluctuations at $(x, y_0^+ = 102, z)$ and spanwise polymer torque fluctuations at $(x+r_x, r_y, z+r_z)$ for (*a*) DR = 18 % and (*b*) DR = 61 %. Contours are plotted in the x–y plane at $r_z^+ = 0$. The increment of contour levels is 0.05. Negative contours are dashed and zero contours are not drawn. Flooded contours represent $R_{\omega_z'\omega_z'}$.

smaller. *In general, the coherent vortices in DR flow are bigger, weaker and* (*from inspection of realization of the random fields*) *less numerous.*

The effects of polymer stresses on the turbulence have been investigated by examining the polymer work term in the Reynolds stress budget equations. The streamwise polymer work is positive very close to the wall, but changes its sign to be negative away from the wall. However, the cross-stream components always have negative values across the whole channel. The behaviour of the polymer work term is consistent with the previous findings of de Angelis *et al.* (2002). The conditionally averaged fields for the events with large contribution to the polymer work show that the vortical structures related to the large events contributing to polymer work are very similar to those for the Q2 events. This verifies that the interaction between added polymer stresses and the conditional eddy structures are important in polymer drag-reducing flows.

It is found that the distributions of conditionally averaged polymer force and torque around the three-dimensional conditional eddy structures associated with Q2 events retard the vortex motion. The concept of vortex retardation by polymer forces was introduced in the study of the energetics of fully turbulent flow with polymer forces by de Angelis *et al.* (2002) and Dubief *et al.* (2005), and in the work of Stone *et al.* (2004) for the quasi-streamwise vortices found in exact coherent states at relatively low Reynolds number. The present work extends the concept of vortex retardation by polymer forces in fully turbulent wall flow by relating the three-dimensional structure

of the conditional eddies to the structure of the polymer force fields associated with them. Our results confirm and add scope to the conclusions of earlier work. Further, we have shown that the polymer forces inhibit the Q2 pumping of the hairpin vortex as well as the ejection/sweep motions at the flanks of quasi-streamwise vortices in the buffer layer. The retardation of Q2 events associated with hairpins is a new mechanism.

The simplest explanation of vortex retardation rests in the relationship between the vorticity and the torque caused by polymer stresses. Our most important finding is that the vortex motions of both the quasi-streamwise vortices and the hairpin vortices create viscoelastic stresses whose torques, $\nabla \times (\nabla \cdot \boldsymbol{\tau})$, inherently oppose the rotation of the vortices. This idea is similar to the concept of eddy damping by polymer forces, but it more specifically addresses the source of the Reynolds stress damping, which lies in counter-torques applied to the vortices responsible for generation of Reynolds shear stresses.

The weakening of the vortices by polymer torques and the accompanying increase in their size explain part of the decrease in Reynolds shear stress production and skin friction. But, visualizations also indicate that the number of vortices in DR flows is also reduced, and some portion of the reduction of Reynolds shear stress and drag must also be attributable to this effect. Hence, the vortex retardation mechanism may not by itself provide a complete explanation of drag reduction by polymers. Further work is needed to see how the retardation affects the creation and destruction of vortices and the equilibrium number density of the vortex population.

This work was supported by Office of Naval Research through contract N000140510687. KK would like to acknowledge the financial support by the Korea Research Foundation Grant (KRF-2005-214-M01-2005-000-10056-00). C.F.L would like to acknowledge the financial support from National Natural Science Foundation of China (10672069) and Jiangsu University through a special scientific research fund. R.S. would like to acknowledge NSF grant 0335348.

REFERENCES

Adrian, R. J. 1996 Stochastic estimation of the structure of turbulent flows. In *Eddy Structure Identification* (ed. J. P. Bonnet), pp. 145–196. Springer.

Adrian, R. J., Jones, B. G., Chung, M. K., Hassan, Y., Nithianandan, C. K. & Tung, A. T.-C. 1989 Approximation of turbulent conditional averages by stochastic estimation. *Phys. Fluids* A **1**, 992–998.

Adrian, R. J., Meinhart, C. D. & Tomkins, C. D. 2000 Vortex organization in the outer region of the turbulent boundary layer. *J. Fluid Mech.* **422**, 1–54.

Benzi, R., De Angelis, E., L'vov, V. S., Procaccia, I. & Tiberkevich, V. 2006 Maximum drag reduction asymptotes and the cross-over to the Newtonian plug. *J. Fluid Mech.* **551**, 185–195.

Brooke, J. W. & Hanratty, T. J. 1993 Origin of turbulence-producing eddies in a channel flow. *Phys. Fluids* **5**, 1011–1022.

Chakraborty, P., Balachandar, S. & Adrian, R. J. 2005 On the relationships between local vortex identification schemes. *J. Fluid Mech.* **535**, 189–214.

Choi, H., Moin, P. & Kim, J. 1993 Direct numerical simulation of turbulent flow over riblets. *J. Fluid Mech.* **255**, 503–539.

Choi, H., Moin, P. & Kim, J. 1994 Active turbulence control for drag reduction in wall-bounded flows. *J. Fluid Mech.* **262**, 75–110.

De Angelis, E., Casciola, C. M., L'vov, V. S., Piva, R. & Procaccia, I. 2003 Drag reduction by polymers in turbulent channel flows: Energy redistribution between invariant empirical modes. *Phys. Rev.* E **67**, 056312.

De Angelis, E., Casciola, C. M. & Piva, R. 2002 DNS of wall turbulence: Dilute polymers and self-sustaining mechanisms. *Comput. Fluids* **31**, 495–507.

Dimitropoulos, C. D., Sureshkumar, R. & Beris, A. N. 1998 Direct numerical simulation of viscoelastic turbulent channel flow exhibiting drag reduction: Effect of the variation of rheological parameters. *J. Non-Newtonian Fluid Mech.* **79**, 433–468.

Dimitropoulos, C. D., Sureshkumar, R., Beris, A. N. & Handler, R. A. 2001 Budget of Reynolds stress, kinetic energy and streamwise enstrophy in viscoelastic turbulent channel flow. *Phys. Fluids* **13**, 1016–1027.

Dubief, Y., Terrapon, V. E., White, C. M., Shaqfeh, E. S. G., Moin, P. & Lele, S. K. 2005 New answers on the interaction between polymers and vortices in turbulent flows. *Flow, Turbulence and Combustion* **74**, 311–329.

Dubief, Y., White, C. M., Terrapon, V. E., Shaqfeh, E. S. G., Moin, P. & Lele, S. K. 2004 On the coherent drag-reducing and turbulence-enhancing behavior of polymers in wall flows. *J. Fluid Mech.* **514**, 271–280.

Ganapathisubramani, B., Longmire, E. K. & Marusic, I. 2003 Characteristics of vortex packets in turbulent boundary layers. *J. Fluid Mech.* **478**, 35–46.

Gupta, V. K., Sureshkumar, R. & Khomami, B. 2005 Passive scalar transport in polymer drag-reduced turbulent channel flow. *AIChE J.* **51**, 1938–1950.

Housiadas, K. D., Beris, A. N. & Handler, R. A. 2005 Viscoelastic effects on higher order statistics and on coherent structures in turbulent channel flow. *Phys. Fluids* **17**, 035106.

Kendall, T. M. 1992 Dynamics of conditional vortices in turbulent channel flow: A direct numerical simulation. Master's thesis, University of Illinois, Urbana, Illinois.

Li, C.-F., Sureshkumar, R. & Khomami, B. 2006*a* Influence of rheological parameters on polymer induced turbulent drag reduction. *J. Non-Newtonian Fluid Mech.* **140**, 23–40.

Li, W., Xi, L. & Graham, M. D. 2006*b* Nonlinear travelling waves as a framework for understanding turbulent drag reduction. *J. Fluid Mech.* **565**, 353–362.

Lim, J., Choi, H. & Kim, J. 1998 Control of streamwise vortices with uniform magnetic fluxes. *Phys. Fluids* **10**, 1997–2005.

L'vov, V. S., Pomyalov, A., Procaccia, I. & Tiberkevich, V. 2004 Drag reduction by polymers in wall bounded turbulence. *Phys. Rev. Lett.* **92**, 244503.

Min, T., Yoo, J. Y. & Choi, H. 2003*a* Maximum drag reduction in a turbulent channel flow by polymer additives. *J. Fluid Mech.* **492**, 91–100.

Min, T., Yoo, J. Y., Choi, H. & Joseph, D. D. 2003*b* Drag reduction by polymer additives in a turbulent channel flow. *J. Fluid Mech.* **486**, 213–238.

Moehlis, J., Faisst, H. & Eckhardt, B. 2004 A low-dimensional model for turbulent shear flows. *New J. Phys.* **6**, 56.

Moin, P., Adrian, R. J. & Kim, J. 1987 Stochastic estimation of organized structures in turbulent channel flow. In *Proc. 6th Turbulent Shear Flow Symp.*, pp. 16.9.1–16.9.8.

Oldaker, D. K. & Tiederman, W. G. 1977 Spatial structure of the viscous sublayer in drag-reducing channel flows. *Phys. Fluids* **20**, 133–144.

Peterlin, A. 1961 Streaming birefringence of soft linear macromolecules with finite chain length. *Polymer* **2**, 257–291.

Ptasinski, P. K., Boersma, B. J., Nieuwstadt, F. T. M., Hulsen, M. A., Van den Brule, B. H. A. A. & Hunt, J. C. R. 2003 Turbulent channel flow near maximum drag reduction: Simulations, experiments and mechanisms. *J. Fluid Mech.* **490**, 251–291.

Ptasinski, P. K., Nieuwstadt, F. T. M., Van den Brule, B. H. A. A. & Hulsen, M. A. 2001 Experiments in turbulent pipe flow with polymer additives at maximum drag reduction. *Flow, Turbulence and Combustion* **66**, 159–182.

Robinson, S. K. 1991 Coherent motions in the turbulent boundary layer. *Annu. Rev. Fluid Mech.* **23**, 601–639.

Roy, A., Morozov, A., van Saarloos, W. & Larson, R. G. 2006 Mechanism of polymer drag reduction using a low-dimensional model. *Phys. Rev. Lett.* **97**, 234501.

Sreenivasan, K. R. & White, C. M. 2000 The onset of drag reduction by dilute polymer additives, and the maximum drag reduction asymptote. *J. Fluid Mech.* **409**, 149–164.

Stone, P. A., Roy, A., Larson, R. G., Waleffe, F. & Graham, M. D. 2004 Polymer drag reduction in exact coherent structures of plane shear flow. *Phys. Fluids* **16**, 3470–3482.

Stone, P. A., Waleffe, F. & Graham, M. D. 2002 Toward a structural understanding of turbulent drag reduction: Non-linear coherent states in viscoelastic shear flows. *Phys. Rev. Lett.* **89**, 208301.

Sureshkumar, R., Beris, A. N. & Handler, R. A. 1997 Direct numerical simulation of the turbulent channel flow of a polymer solution. *Phys. Fluids* **9**, 743–755.

Terrapon, V. E., Dubief, Y., Moin, P., Shaqfeh, E. S. G. & Lele, S. K. 2004 Simulated polymer stretch in a turbulent flow using Brownian dynamics. *J. Fluid Mech.* **504**, 61–71.

Virk, P. S. 1971 An elastic sublayer model for drag reduction by dilute solutions of linear macromolecules. *J. Fluid Mech.* **45**, 417–440.

Virk, P. S., Merrill, E. W., Mickley, H. S., Smith, K. A. & Mollo-Christensen, E. L. 1967 The Toms phenomenon: Turbulent pipe flow of dilute polymer solutions. *J. Fluid Mech.* **30**, 305–328.

Waleffe, F. 1997 On a self-sustaining process in shear flows. *Phys. Fluids* **9**, 883–900.

Warholic, M. D., D. K. Heist, M. K. & Hanratty, T. J. 2001 A study with particle-image velocimetry of the influence of drag-reducing polymers on the structure of turbulence. *Exps Fluids* **31**, 474–483.

Warholic, M. D., Massah, H. & Hanratty, T. J. 1999 Influence of drag-reducing polymers on turbulence: Effects of Reynolds number, concentration and mixing. *Exps Fluids* **27**, 461–472.

Wei, T. & Willmarth, W. W. 1992 Modifying turbulent structure with drag-reducing polymer additives in turbulent channel flows. *J. Fluid Mech.* **245**, 619–641.

White, C. M., Somandepalli, V. S. R. & Mungal, M. G. 2004 The turbulence structure of drag reduced boundary layer flow. *Exps Fluids* **36**, 62–69.

Willmarth, W. W., Wel, T. & Lee, C. O. 1987 Laser anemometer measurements of Reynolds stress in a turbulent channel flow with drag reducing polymer additives. *Phys. Fluids* **30**, 933–935.

Zhou, J., Adrian, R. J., Balachandar, S. & Kendall, T. M. 1999 Mechanisms for generating coherent packets of hairpin vortices. *J. Fluid Mech.* **387**, 353–396.